Using pulsed neutron transmission for crystalline phase imaging and analysis

Journal Item

Using pulsed neutron transmission for crystalline phase imaging and analysis

A. Steuwer[a] and P. J. Withers
Materials Science Centre, University of Manchester, Grosvenor Street, Manchester M1 7HS, United Kingdom

J. R. Santisteban and L. Edwards
Department of Materials Engineering, Open University, Milton Keynes MK7 1AA, United Kingdom

(Received 19 August 2004; accepted 10 December 2004; published online 22 March 2005)

The total scattering cross section of polycrystalline materials in the thermal neutron region contains valuable information about the scattering processes that neutrons undergo as they pass through the sample. In particular, it displays characteristic discontinuities or Bragg edges of selected families of lattice planes. We have developed a pixelated time-of-flight transmission detector able to record these features and in this paper we examine the potential for quantitative phase analysis and crystalline phase imaging through the examination of a simple two-phase test object. Two strategies for evaluation of the absolute phase volumes (path lengths) are examined. The first approach is based on the evaluation of the Bragg edge amplitude using basic profile information. The second approach focuses on the information content of certain regions of the spectrum using a Rietveld-type fit after first identifying the phases via the characteristic edges. The phase distribution is determined and the coarse chemical species radiographic image reconstructed. The accuracy of this method is assessed. © *2005 American Institute of Physics*. [DOI: 10.1063/1.1861144]

I. INTRODUCTION

Using a transmission detector one can measure the change in intensity brought about by the insertion of the sample in the beam.[1] In principle, the transmission spectrum contains information about all the different scattering and reaction processes that have occurred in the sample. The spectrum, or rather the total scattering cross section, displays an intricate pattern in the thermal regime where coherent elastic scattering dominates for many materials.[2,3] As an essentially energy dispersive technique, the framework of time-of-flight[4] provides the possibility of investigating the spectra conveniently and directly as a function of neutron wavelength. There has been a long history of measuring fundamental properties by neutron transmission, but except for radiography, transmission techniques have never really found their way into mainstream application. The scope of transmission techniques are inherently limited to features defined by the detector resolution and sample sizes defined by the scattering properties and path length (thickness) of the sample or constituent phase. The intensity of neutron beams and the efficiency and spatial resolution of new detectors[5] at spallation sources have led to a reappraisal of transmission techniques opening up the possibility of basic crystalline phase imaging (radiography), and thereby implicitly tomography. Transmission measurements have already been used successfully to monitor phase transformations and relative phase volume fractions in metals[6–9] but usually complementary methods have been relied upon for the calibration of phase volume fractions. A combination of both imaging and diffraction with a pixelated time-of-flight (TOF) transmission detector would allow time and spatially resolved monitoring of phase transitions, with the possibility of fast quantitative phase analysis.

In this paper, we outline a framework for extracting phase information quantitatively, and show how TOF neutron transmission can be used to undertake spectroscopic radiography. We analyze certain features of the transmission spectrum in the thermal region of 0.5–5.5 Å, based on a semiempirical approach. We determine the phase volume fraction of a simple two-phase test object containing iron and copper via a twofold approach. First, using the amplitude of the Bragg edges as the basic measure of phase volume, and secondly based on a whole-pattern, Rietveld-type refinement approach.[10] Additionally we present the results of applying a phase filtering technique to the data to obtain phase contrast images. A few preliminary results of the material presented in this paper have already been presented to the European Conference on Neutron Scattering in Montpellier (2003), and have been published in Ref. 11.

II. THEORETICAL BACKGROUND

For a sufficiently polycrystalline material (that is for a material which contains many randomly oriented grains) placed in a neutron beam there will always be a subset of suitably aligned grains that diffract these neutrons of a given wavelength into the appropriate scattering cone at an angle 2θ. The resulting reduction in transmission intensity $I_{tr}(\lambda)$ to the incident intensity $I_{in}(\lambda)$ is given by the general relation

$$I_{tr}(\lambda) = I_{in}(\lambda)\exp(-N_c w \sigma_{tot}(\lambda)), \quad (1)$$

where λ is the neutron wavelength, N_c the number of atoms per unit volume, and σ_{tot} is the atomic total scattering cross section.[1] The quantity $T_w = \exp(-N_c w \sigma_{tot})$ is also known as

[a]Electronic address: steuwer@ill.fr. Currently at: FaME38 at the ESRF-ILL, 6 Rue J. Horowitz, 38042 Grenoble, France.

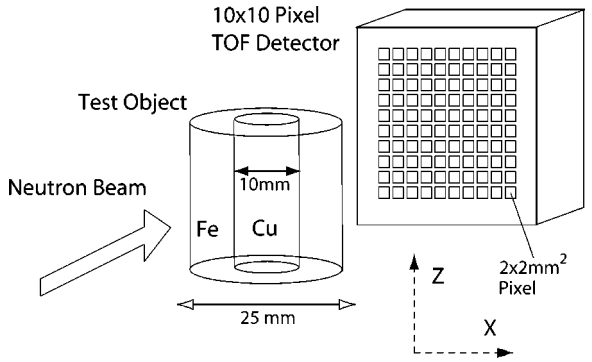

FIG. 1. A schematic of the experimental set-up and the test object. The test object was placed in front of the pixelated transmission detector. Two images have been recorded, in between which the sample was translated horizontally by half the pixel spacing (1.25 mm) perpendicular to the beam.

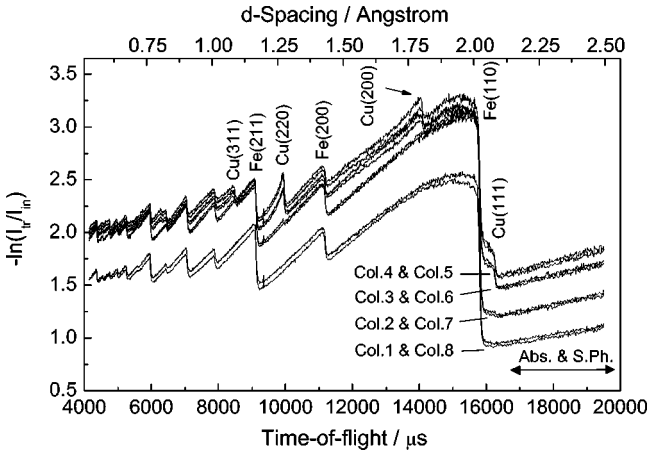

FIG. 2. The transmission spectrum (total scattering cross section) for each of the eight columns for the first sample position. Only the central four columns exhibit Cu edges, accompanied by a strong increase in the absorption rate.

the transmission factor and describes the probability that a neutron will be transmitted a distance w. The total cross section is obtained from the measured spectra by inverting Eq. (1). Practically, it is often more convenient to use the so-called macroscopic cross sections, e.g., $\Sigma_{\mathrm{coh}}(\lambda)w = N_c w \sigma_{\mathrm{coh}}(\lambda)$, which describe the bulk properties of the material. The macroscopic cross sections can be defined as $\Sigma = N_c\sigma = N_A\rho\sigma/A = \sigma/v_0$, where $N_A = 0.6022 \times 10^{24}$ is Avogadro's number, ρ the density of the material, A its atomic weight, and v_0 the volume of the unit cell.[12,13] Similar to linear attenuation constants in conventional x-ray diffraction, they are quoted in units of cm^{-1}. Optionally, one can include a scale factor $s = \rho/\rho'$ which takes into account the difference between actual and theoretical density of the specimen, e.g., for powders. At short path lengths both the scattering and attenuation processes suffer from low signal. With increasing path length the coherent scattering becomes more significant (depending on the scattering length) because the number of scattering centers increases drastically. However, further increases in path length also gives rise to considerable attenuation and eventually the coherent scattering fingerprint becomes suppressed by the overall loss of signal due to subsequent attenuation.

The many different contributions to the total scattering cross section have been discussed and derived in great detail elsewhere.[2,14–16]

Other scattering effects, such as small angle scattering, extinction, and second order, multiple-scattering events are not insignificant for the current experimental set-up and sample geometry, but a comprehensive discussion is beyond the scope of this paper. In the following, we review only the basic factors affecting the transmitted intensity for a simple iron–copper test object in order to examine the feasibility of crystalline phase imaging and quantitative analysis (see Fig. 1).

A. The coherent elastic scattering

Quantitative phase analysis methods often use the intensity of a Bragg peak as a measure of the amount of material of a particular phase in the specimen. Coherent elastic or Bragg scattering, which is the cause for these peaks, is described by the Bragg equation and can be formulated for the transmission geometry. In TOF, for a given *hkl*-reflection the scattering angle approaches $2\theta = 180°$ with increasing wavelength until a fraction of the incident neutrons is completely backscattered towards the source. At this point the diffracting lattice planes are aligned so that their plane normal is parallel to the beam. For longer wavelengths, Bragg diffraction from this particular set of lattice plane spacings can no longer occur. This is accompanied by a sudden increase (a Bragg edge) in the transmitted intensity, and equivalently a drop in the scattering cross section. As a result, the position of each Bragg edge corresponds to a particular lattice spacing characteristic of the crystal structure of the sample, as indicated in Fig. 2. In the framework of TOF one obtains for Bragg's equation in transmission

$$\lambda = 2d = \frac{h}{m_n L} t, \tag{2}$$

where L is the length of the flight path, m_n the neutron mass, h is Planck's constant, and t the time elapsed before the neutron is detected. Hence, for a particular *hkl* reflection with *d*-spacing d_{hkl}, the Bragg edge position can be expressed without loss of generality in a TOF equivalent as t_{hkl}. A Bragg edge in the total cross section is formed when one family of lattice planes ceases to contribute to the scattering, as described by Eq. (2). For the lowest possible reflection, this is commonly known as the Bragg cut-off. As a result, the coherent elastic scattering cross section contains important information about the crystalline state of the sample. In the thermal regime for a texture-free polycrystalline solid it is given by

$$\sigma_{\mathrm{coh}}^{\mathrm{el}}(\lambda) = \frac{\lambda^3}{2v_0 \sin\theta} \sum_{hkl} M_{hkl} |F_{hkl}|^2 D_{hkl} H(2d_{hkl} - \lambda), \tag{3}$$

where D_{hkl} is the usual Debye–Waller factor and F_{hkl} is the structure factor of the unit cell for the *hkl*-reflection.[1] For the sake of simplicity later, we have chosen to separate the Debye–Waller factor and the structure factor, which to the degree of accuracy aimed at in this paper should be permissible. Also, by using a multiplicity factor M_{hkl} the sum in Eq.

(3) is over all symmetry related reflections *hkl*. The Heaviside step-function H ensures that the the Bragg constraint $2d \geqslant \lambda$ is fulfilled, and provides the basic theoretical edge profile. Each Bragg edge amplitude only depends on the coherent elastic scattering of one family *hkl* of lattice planes which suddenly ceases to scatter neutrons from the beam, as the other cross sections are slowly varying functions over the small wavelength range of a Bragg edge.[17] In practice, a particular edge, say at t_0 has a finite width and a distinct profile as a function of $\tau = t - t_0$. Typically, it can be refined[18,19] using a normalized integral of a Gaussian $G(t, \sigma_G)$ convoluted with a cut-off decaying exponential $[E(t, \alpha) = \exp(-\alpha t), t \geqslant 0; E(t, \alpha) = 0, t < 0]$ to give it the characteristic asymmetry[20,21] arising from the pulsed nature of the way neutrons are produced,

$$B(\tau, \sigma_G, \alpha) = \int_{-\infty}^{\tau} G(t, t_0, \sigma_G) \otimes E(t, t_0, \alpha) dt. \tag{4}$$

Therefore each Bragg edge has a characteristic set of profile parameters (amplitude, width, and position) analogous to a conventional Bragg peak. This opens up the possibility of applying the whole-pattern decomposition techniques of conventional powder diffraction[22,23] in order to extract information from the spectrum. In the case of relative phase volume fraction determination, given a suitable implementation of the profile around the edge, each observed Bragg edge profile contribution b_{ci}, where the subscript i indicates the ith data point in the profile, can be expressed in a similar fashion to Eq. (3) in Ref. 24 as

$$b_{ci} = S M_{hkl} |F_{hkl}|^2 D_{hkl} B_i \tag{5}$$

with a scale factor $S = (N_c \lambda^3 / 4 v_0) w$. This scale factor is refined during the fitting of the Bragg edge, and proportional to the phase (volume) path length w. Considering the finite area A_D of each detector pixel, this determines the total mass $(\approx A_D w N_A \rho)$ of the phase along the beam path. The concept of a phase volume is therefore equivalent to that of a phase *path length* for the transmission geometry. The generalization to a multiphase system (and powders) is straightforward. The relative phase path lengths w_i are then given by $w_i = S_i / \Sigma_j S_j$. In the case of absolute phase volume fraction determination, using basic assumptions about the crystallographic structure of the phases from the observed patterns, the theoretical Bragg edge amplitude $\Delta_{hkl} = (\Sigma_{\mathrm{coh}}^{\mathrm{el}} w)_{hkl}$ of a particular Bragg edge *hkl* in the normalized spectrum can be used to estimate the amount of that particular phase.

Practically, this can be achieved by fitting a step-function discontinuity in the vicinity of the Bragg edge instead of the asymmetric Bragg edge profile $B(\tau, \sigma_G, \alpha)$ described above (equivalent to having no instrumental or sample broadening). The measured edge amplitude (as cross section) amplitude Δ_{hkl} is given by the particular *hkl*-term contributing to $\Sigma_{\mathrm{coh}}^{\mathrm{el}}(\lambda)$ only. Therefore one can estimate the absolute path length w from Eq. (3) for a bcc material as

$$w = \frac{A n^{3/2} \Delta_{hkl}}{4 b^2 D_{hkl} M_{hkl} N_A \rho} = C \times \frac{n^{3/2} \Delta_{hkl}}{D_{hkl} M_{hkl}}, \tag{6}$$

where $n^2 = h^2 + k^2 + l^2$ is the index of the reflection, A is the atomic number of the single-phase element, and because for a bcc crystal, the structure factor reduces to $|F_{hkl}|^2 = (2b)^2$ if the sum $h + k + l$ is an even number and zero otherwise. [Equally, for fcc materials, this reads $|F_{hkl}|^2 = (4b)^2$, for h, k, l all even or all odd.] Since for each spectrum the path length and scattering properties of the sample are constant, the dimensionless quantity $f_{hkl} = n^{3/2} \Delta_{hkl} / D_{hkl} M_{hkl}$ has to yield the same numeric value for all edges, and is proportional to the path length of the underlying phases. The quantity $C = A / 4 b^2 N_A \rho$ in Eq. (6) carries the unit length, and defines the proportionality between observed Bragg edge amplitude and phase volume (path length). It is here that more specific assumptions about the nature of the phases have to be made. For our (almost) pure Fe and Cu test object, C has the values $C_{\mathrm{Fe}} = 3.27$ cm and $C_{\mathrm{Cu}} = 4.96$ cm, respectively. If many Bragg edges are fitted separately to evaluate the path length Eq. (6) extends to $w = \pi (\sigma_c N_c)^{-1} \langle f_{hkl} \rangle$, where $\sigma_c = 4 \pi b^2$ and $\langle \cdots \rangle$ can be the normal arithmetic mean. It is always possible, of course to add further constraints which reflect the crystallographic nature of the phase to the fitting of Bragg edge amplitude. It is worth mentioning here that unlike absorption (see Sec. II C) the coherent scattering cross section, strictly speaking the sum of all scattering amplitudes in the unit cell $\sigma_c = 4 \pi |\Sigma_r b_r p_r|^2$, should not be greatly affected by the presence of small amounts of impurities or alloying elements in the sample. Unlike many stainless steels, the ferritic steel used here contains only small amounts of other elements, e.g., typically between 0.6% – 1% of manganese, and less than 1% carbon. It is of course straightforward to write down σ_c if the alloy composition is known.

B. Single-phonon thermal diffuse scattering

It is a common procedure to separate the thermal diffuse scattering (TDS) of phonon excitations into single-phonon and multiple-phonon scattering cross sections, where the latter is only significant for $E \gg k_B T$, and can for the present case be neglected.[25] In the regime beyond the Bragg cut-off the neutrons scatter inelastically mainly through the annihilation of phonons.[26] Following Freund,[25] the scattering cross section for single-phonon scattering σ_{sph} can be expressed as

$$\sigma_{\mathrm{sph}} = \frac{3 \sigma_{\mathrm{bat}}}{A} \left(\frac{k_B \theta_D}{E} \right)^{1/2} \begin{cases} R(x) & x \leqslant 6 \\ 3.3 x^{-7/2} & x \geqslant 6 \end{cases}, \tag{7}$$

where θ_D is the Debye temperature, $x = \theta_D / T$, and σ_{bat} is the sum of the bound coherent and incoherent scattering cross sections. The function $R(x)$ is given by

$$R(x) = \sum_{m=0}^{\infty} \frac{B_m x^{m-1}}{[m\,!\,(m + 5/2)]}, \tag{8}$$

where B_m are the Bernoulli numbers. Evaluating the sum up to $m = 22$, we calculated the single-phonon TDS cross sections at room temperature for Fe and Cu as $\sigma_{\mathrm{sph}}^{\mathrm{Fe}}(\lambda) = 4.01 \times 10^{-25}$ cm^2 Å$^{-1}\lambda$ and $\sigma_{\mathrm{sph}}^{\mathrm{Cu}}(\lambda) = 2.31 \times 10^{-25}$ cm^2

$\text{Å}^{-1}\lambda$ for wavelengths λ larger than given by the Bragg cut-off.

C. Absorption

True absorption (capture) follows with few exceptions the so-called $1/v_n$ law,[1] where v_n is the velocity of the neutron, or expressed as a function of wavelength

$$\sigma_{\text{abs}}(\lambda) = \beta\lambda, \tag{9}$$

where β is a material dependent constant. Since the neutron velocity is inversely proportional to the neutron wavelength, materials appear "harder" to penetrate at long wavelengths than at small wavelengths. As indicated above, the proportionality becomes apparent at wavelengths after the Bragg cut-off of the lowest reflection, Eq. (2), where the absorption term dominates the total cross section, see Fig. 2. The absorption cross section for pure Fe and Cu taken from Ref. 1 are given by $\sigma_{\text{abs}}^{\text{Fe}}(\lambda) = 1.296 \times 10^{-24}\ \text{cm}^2\ \text{Å}^{-1}\lambda$, $\sigma_{\text{abs}}^{\text{Cu}}(\lambda) = 2.04 \times 10^{-24}\ \text{cm}^2\ \text{Å}^{-1}\lambda$. Comparing the magnitude of the absorption cross section with the single-phonon TDS cross section of the previous section one finds that the latter contributes roughly 10% to the linear cross section in the region beyond the Bragg cut-off, see also Ref. 26. The absorption cross section is determined by the predominant material in the beam. But low levels of impurities of strongly neutron absorbing materials such as boron or cadmium can have a profound influence. A simple estimate shows that (a fairly typical amount of) 1% of Mn ($\sigma_{\text{abs}}^{\text{Mn}} = 13 \times 10^{-24}\ \text{cm}^2$ at 1.08 Å) in Fe changes the absorption slope by as much as 5%.

III. THE EXPERIMENT

In this section we describe the essential features of the experimental set-up, i.e., the geometry of the test object and the experimental configuration on ENGIN beam line at ISIS, RAL (UK), where this work was undertaken.

A. The test object

For the purpose of obtaining a set of trial spectral radiographs, a simple test object was constructed. It consisted of a solid copper cylinder of 1 cm diameter and 2.5 cm height shrink-fitted into a hollow ferritic iron (steel) cylinder of the same height but of 2.5 cm outer diameter with a small interference fit at the inner diameter. The shrink-fitting was achieved by cooling the copper cylinder in liquid nitrogen whilst heating the hollow iron cylinder on a hot-plate. The temperature difference and extent of misfit were sufficient to allow an easy shrink-fitting of the copper cylinder into the bore. A schematic of the sample is shown in Fig. 1.

B. Experimental set-up and data preprocessing

The radiography experiment was carried out on the PEARL/ENGIN beamline at the ISIS pulsed neutron spallation source of the Rutherford Appleton Laboratory in the UK. The flight path from source to detector on this beam line is approximately $L = 15.6$ m, and provides a spectral range of neutron wavelengths of around 0.5 – 5 Å. Assuming a lattice parameter of around $a_0 = 2.865$ Å for the ferritic steel, a conversion constant of $h/m_n L = 2.56 \times 10^{-4}\ \text{Å}/\mu\text{s}$ was calculated [see Eq. (2) in sec. II A] for the transformation from TOF to neutron wavelength. The absolute value of this constant is of no relevance for the purpose of the following analysis. If applied to an unknown specimen, the position (in terms of flight path) and calibration of the detector should of course be undertaken independently. A multiple-edge refinement[19] of the copper lattice parameter then yields a lattice parameter of 28100 μs in TOF which corresponds to 3.596 Å, and is in reasonable agreement with the literature values. Pivotal to the approach has been the development of a TOF-sensitive pixelated detector.[27] The detector comprises a 10×10 detector pixel array on a $2.5 \times 2.5\ \text{mm}^2$ pitch, with $A_D = 2 \times 2\ \text{mm}^2$ exposure area per pixel and 0.5 mm thick shielding between each pixel. Due to limitations in the data acquisition hardware, only eight of the ten detector columns were operational during the experiment. Apart from a thin aluminum window over the end of the evacuated beam guides, the detector has an unrestricted view of the moderator. The effect of the aluminum shielding along the beam guides (small Bragg edges) was automatically accounted for during the extraction of the cross section from Eq. (1) using spectra collected without the test object in place (open beam). The sample was placed upright approximately 3 cm in front of the center of the eight columns, with its axis vertical and perpendicular to the direction of the incoming beam, as shown in Fig. 1. The sample to incident slit distance was approximately 400 mm.

The divergence of the beam is approximately 1/150 rad both horizontally and vertically. The time of exposure (counting time) was 45.9 μAh in terms of the proton current per hour at ISIS which is equivalent to approximately 1000 s counting time. The sample was then moved by half the detector spacing (1.25 mm) and measured again in order to improve the lateral spatial resolution. Additionally the unfiltered (open) beam was measured for approximately the same time of exposure. The geometry of the test object means that all the pixels in each column could be added together to reduce count times, and unless otherwise stated, the ten spectra of each column have been added together and the cross sections were extracted using Eq. (1). Each column or pixel has been given a weight proportional to its contribution to the total open beam, in order to account for spatial variations in the incident flux. The raw data has been corrected for the dead-time of the detector of $\tau = 16 \times 10^{-9}$ s, using the relation $N_{\Delta t} = n_{\Delta t}/(1 - n_{\Delta t}\tau)$, where $n_{\Delta t}$ is the number of raw counts for the binning TOF channel Δt and hence $N_{\Delta t}$ is the number of true counts. The small differences in counting times between the two sample positions and the open beam has been corrected for in the preprocessing of the data.

C. The raw experimental spectra

The eight normalized spectra collected for the first sample position are shown in Fig. 2. As expected only the central four columns clearly exhibit Cu Bragg edges.

This is also accompanied by a proportional increase in the absorption rate partly because of the increased path length through the sample and partly because of the larger

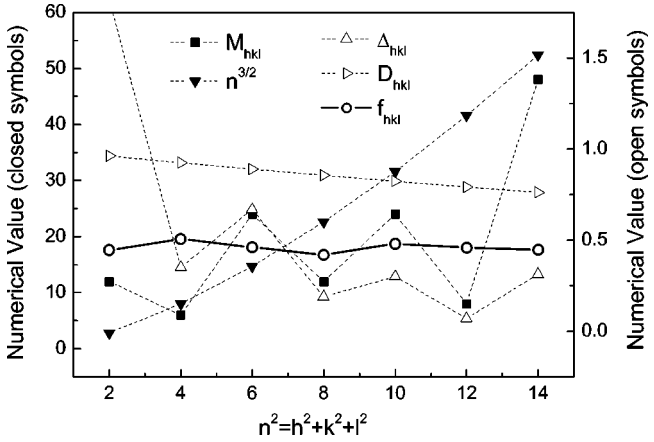

FIG. 3. The quantity $f_{hkl}=n^{3/2}\Delta_{hkl}/D_{hkl}M_{hkl}$, which is proportional to the path length. This has been evaluated for the lowest seven Bragg edges for the iron spectrum of the first pixel column in the detector at position 2.

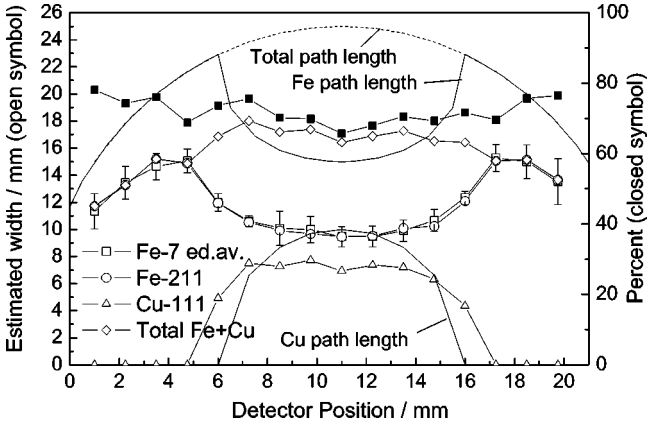

FIG. 4. The absolute path length for Fe and Cu inferred from f_{hkl} using the average of the lowest seven Fe Bragg edges (squares), the strongest and very clear Bragg edge Fe-211 (circles) and Cu-111 (triangles). These are compared with the geometric path lengths (lines).

absorption cross section of Cu over Fe. At times of flight greater than $\approx$16000 μs no Bragg scattering is possible so that only true absorption and a small amount of incoherent scattering contribute significantly to the cross section. From the spectra one can conclude that the sample was indeed centered between column 4 and 5. On the basis of the sample dimensions the geometrical estimate of the average total path lengths for the first and last four columns are approximately: col. 1 and col. 8=17.8 mm, col. 2 and col. 7=21.6 mm, col. 3 and col. 6=23.8 mm, col. 4 and col. 5=24.9 mm.

IV. ANALYSIS

Here we shall examine the extent to which geometrical and compositional information about the test object can be extracted from the transmission spectra. To reiterate, since the detector position is fixed and calibrated, the relation between TOF and neutron wavelength is known. Therefore, the two phases can be unambiguously identified as one phase having the bcc structure with a lattice parameter of around 2.865 Å and one phase having the fcc structure with a lattice parameter of around 3.59 Å. These two phases can be identified as iron (Fe) and copper (Cu), the latter showing a significant amount of texture as apparent in the shape of the Cu edges in the spectra of the central columns in Fig. 2. The quantitative analysis of the respective path length (phase volume fraction) as a function of the spatial position is now undertaken following two approaches, first from the measured amplitude of the Bragg edges directly, and second from a whole-pattern refinement approach restricted to a certain region of the spectrum.

A. Fitting the Bragg edges

After preprocessing and normalizing the data in the way described above, we analyze the Bragg edges separately in the different spectra. Following the procedures outlined in Sec. II, Fig. 3 shows the measured edge amplitude Δ_{hkl}, the calculated Debye–Waller factor D_{hkl}, as well as the crystallographic parameters $n^{3/2}, M_{hkl}$ for the lowest seven Bragg edges of the iron spectrum collected on pixel column 1 for the second position of the sample. As expected, the estimated value of $f_{hkl}=0.46$ is approximately equal for all seven edges, and gives an estimate of the absolute path length $w_{\mathrm{Fe}}=15.1$ mm for iron. (At this location, there are no copper Bragg edges in the spectrum.) In Fig. 4 the absolute path lengths are shown as estimated from an average over the lowest seven Bragg edge for the Fe phase, and from the Fe-211 Bragg edge alone, as well as estimated from the Cu-111 edge. The estimated path lengths are also compared with the "real" path length calculated from the cylinder geometry.

The average over the seven lowest Bragg edges of Fe gives almost identical results to that determined from the Fe-211 Bragg edge only. These inferred path lengths compare reasonably with the geometrical results quoted.

Quantitatively, the inferred absolute path lengths fall short of the geometrical values by approximately 30%. The fact that each measurement point in Fig. 4 shows a similar discrepancy indicates a systematic rather than experimental error (in this case for both phases). This indicates that the basic model for the Bragg edge amplitude requires some correction.

Qualitatively, as shown in Fig. 5 the derived relative path lengths agree very well with the expected profile and symmetry.

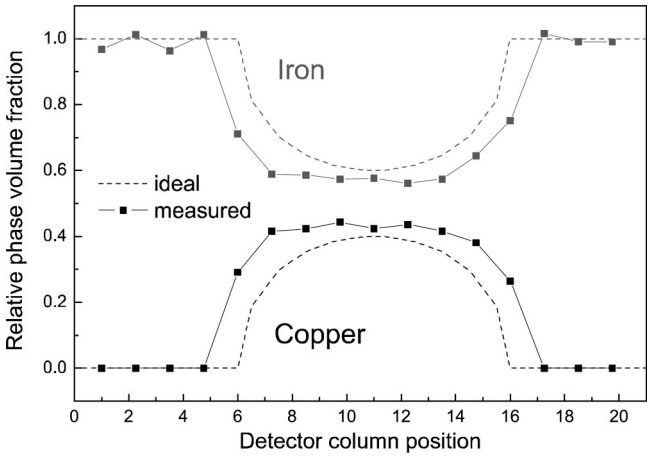

FIG. 5. The estimated relative phase volume fractions for Fe and Cu estimated in terms of the quantity f_{hkl} using $w_i=S_i/\Sigma S_i$.

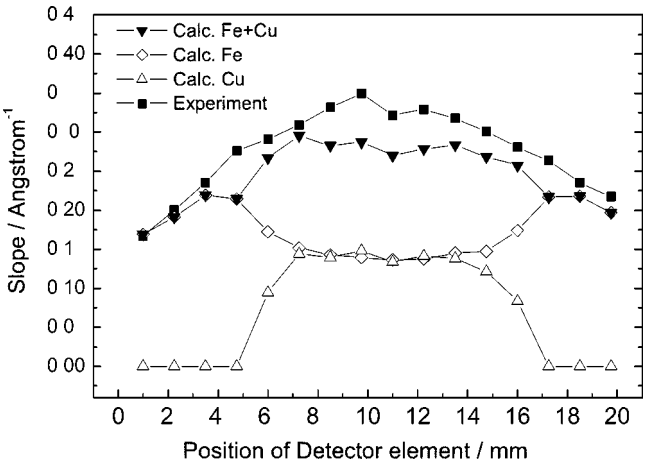

FIG. 6. The slopes (absorption plus single-phonon contribution) calculated using the path lengths estimated from the Bragg edges Fe-211 and Cu-111 compared with the fitted values from the region beyond the Bragg cut-off.

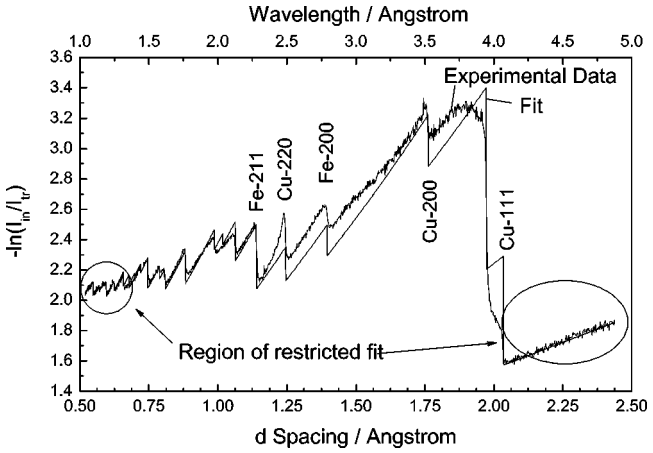

FIG. 7. An example of the experimental data (col. 4, position 1) fitted with a theoretical spectrum, highlighting approximately the restricted area of the fit. Note the effect of strong texture in the Cu Bragg edges, e.g., Cu-220 compared to Fe-211.

Both relative and absolute path lengths indicate a larger diameter of the Cu core than was used. This has been attributed to the divergence of the beam and possible scattering of neutrons into neighboring pixels and suggests the use of secondary collimators or Soller slits between sample and detector.

Having calculated the absorption and TDS cross section in Sec. II C, the measured Bragg edge amplitude (equivalent to the amount of material of a phase along the beam path) can be used to calculate the slope in the absorption tail of the spectrum and compare it to experimental values. Fitting a linear equation to the absorption tail (in the region of the spectrum beyond the lowest reflection $\lambda \geqslant 4.2$ Å, the results for our two phase-system are compared in Fig. 6.

For convenience, we quote here the factor $N_c(\mathrm{Fe}) = 0.08489 \times 10^{24}\ \mathrm{cm}^{-3}$ and $N_c(\mathrm{Cu}) = 0.084662 \times 10^{24}\ \mathrm{cm}^{-3}$, which can be set equal to $0.0847 \times 10^{24}\ \mathrm{cm}^{-3}$ for both materials in this context (and to our accuracy). The calculated slopes are within reasonable agreement with the measured slopes, and follow the trend observed in Fig. 4. On average, the calculated slopes agree to roughly 89% with the experimentally determined slopes. This suggests that a correction to either the estimate from the Bragg edge amplitude or to the predicted slope should be undertaken for full consistency.

B. Restricted Rietveld fitting

Given the knowledge of the scattering contributions to the total cross section, it is possible to undertake a whole-pattern fitting in the sense of a Rietveld-type fit using the basic properties of the phases one has identified in the spectrum, including the theoretical cross sections described above. Using the implementation contained within the software routines CRIPO (Ref. 16) for the thermal region, which contains the basic coherent and incoherent, elastic and inelastic scattering cross sections, we fitted the measured spectrum restricted to the short and long wavelength region of the spectra. Since the total cross section for the region towards the lowest reflections is highly complex and fitting requires a correct model description of inelastic scattering, as well micro-structural properties such as texture, etc., this region was excluded from the fitting procedure. As a result, this approach does not involve a direct estimation of the phase volume fraction through the amplitude of the Bragg edge, and therefore represents an independent, complementary approach to that in Sec. IV A. However, the restricted fit still contains a significant contribution from the coherent elastic scattering cross section in the short wavelength limit. Texture effects become negligible in the short wavelength region and, of course, do not occur beyond the Bragg cutoff wavelength region. Furthermore, the approximation to the inelastic scattering in the short wavelength region becomes increasingly better.[28,16] An example of such a fit is shown in Fig. 7. As is evident from Fig. 7, the profile of the Cu-111 and Cu-220 Bragg edges are strongly affected by texture, which would make an accurate whole-pattern fit without a proper model very difficult.

Using the restricted Rietveld fitting approach, the transmission (diffraction) pattern is calculated by adding the total scattering cross sections of iron and copper, and subsequent varying of the respective path lengths. By allowing the respective number of scattering centers along the beam path to vary, one can estimated the absolute path length of each phase.

Figure 8 shows the absolute path length estimated from such a restricted Rietveld fit to the measured spectra. Again, qualitatively, the estimated path lengths follow the expected profile given the sample geometry, and a graph of the relative path length similar to that of Fig. 5 has been omitted for sake of brevity.

Unlike the individual Bragg edge analysis of Sec. IV A the copper path length is slightly overestimated. This can be in part explained by the fact that the fitting routine does not consider impurities and normal noise. Since Cu has a larger incoherent scattering cross section, any background noise (not included in the model) is more likely to be attributed as Cu. However, quantitatively the path length again underestimates the total actual thickness. The ratio between estimated and measured total absolute path lengths is fairly constant at approximately 87(1)%, as shown by the closed symbols in Fig. 8. While most of our analysis has focused on data

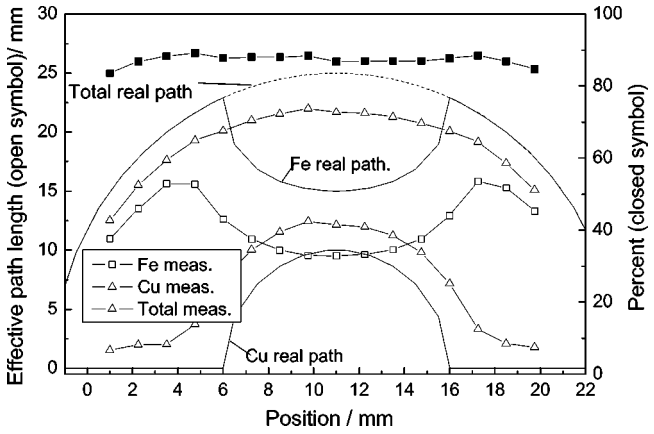

FIG. 8. The thickness of the sample estimated by fitting a theoretical profile to the measured data in the short and long wavelength (beyond the cut-off) limit. Also shown is the ratio of estimated and calculated path length as percent (right scale).

summed over all the pixels in each column of our pixelated detector to get a good estimate of the Bragg edge amplitude, the signals recorded by each pixel are sufficient for pixel-by-pixel imaging using the restricted Rietveld analysis approach. The results from the fit are shown in Fig. 9. As expected, the variation across the sample is almost identical for all 10 rows. The estimated path lengths calculated using the pixel-by-pixel analysis are of course similar to that of the column-averaged spectra (approximately 93% of the true value). The total path length in Fig. 9 (bottom) is faithful to the cylindrical shape of the test object.

V. CRYSTALLINE PHASE IMAGING

The analysis of the previous sections leads naturally to the concept of radiography. Radiography, or tomography, involves the study of the spatial variation of the absorption or attenuation (i.e.; transmission factor) of radiation. For pulsed neutron transmission, the energy-selective discrimination of the attenuation comes naturally, and "radiographs" can in principle be evaluated for every wavelength (energy) in the spectrum. In a related approach,[29] calculated the minimum detectable mass based on a change in the macroscopic cross section for different neutron wavelengths (energies). By comparing the relative intensities (total scattering cross section) just before and after a Bragg edge associated with a particular (inferred) phase, one can introduce the concept of "phase filters," e.g., for Fe-200 at $\lambda = 4.05 \pm 0.05$ Å. If the associated phase is present along a particular beam path, then there will be a noticeable difference in the total cross section due to the presence of a Bragg edge provided that the it is not suppressed by, e.g., texture or has a very small structure factor etc. If not, then this difference will be negligible.

This is demonstrated in Fig. 10. In this case, the 10×16 spectra (for both sample positions) have been analyzed pixel-by-pixel to obtain the radiographs shown. The gray-level is proportional to the relative difference in the value of the total scattering cross section in the immediate vicinity of a Bragg edge. Applying no filter is essentially equivalent to the average (summed) cross section. Of course, these filters only apply to (crystalline) phases which have a significant

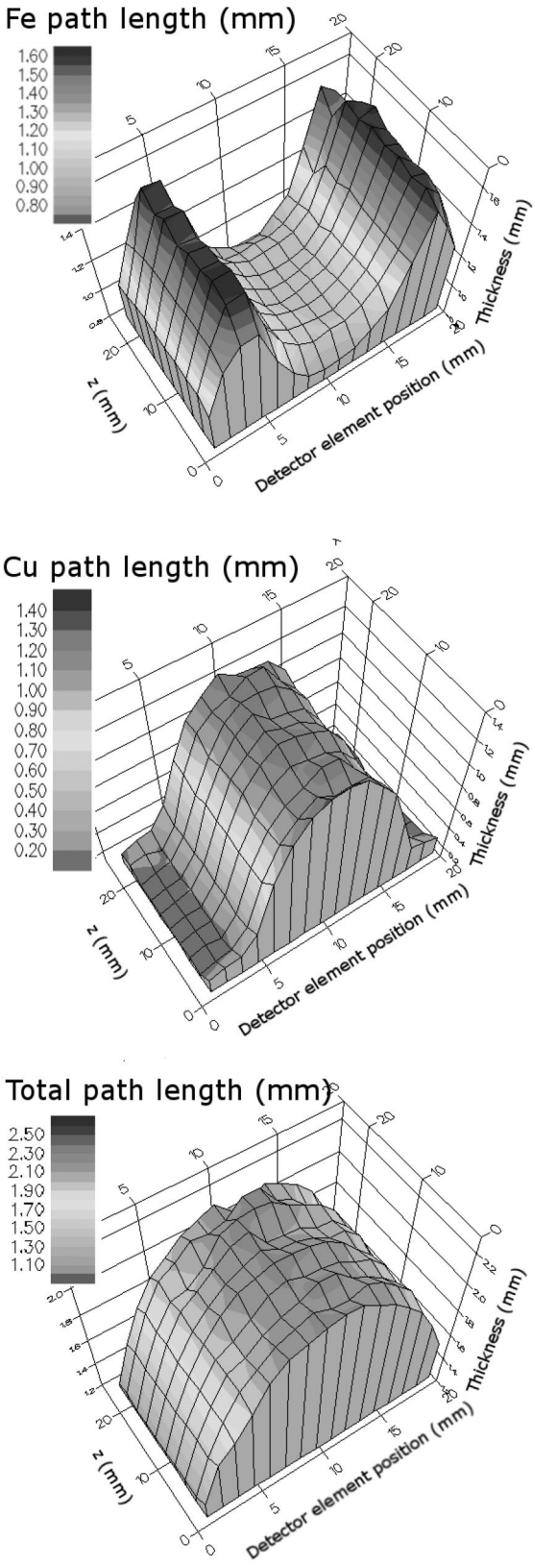

FIG. 9. The estimated path length for each pixel by applying the restricted Rietveld fit, for Fe (top), Cu (middle), and the combined path length (bottom).

contribution to the coherent elastic scattering cross section, i.e., where the Bragg edge amplitude is larger than the background noise. The extension to a tomographic analysis is straightforward.

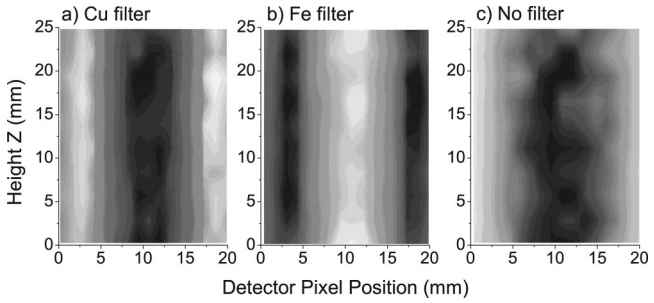

FIG. 10. Pixel-based (10×16) radiographs using a Fe-211 filter (a), a Cu-220 filter (b), and no filter (c); see also Fig. 9 for comparison. The darker shades indicate more path length (opacity).

VI. DISCUSSION AND CONCLUSIONS

We have presented the basic framework and demonstrated the applicability of the pulsed neutron transmission method towards phase determination and simple crystalline phase imaging by analyzing the transmission spectra of a simple two-phase Fe–Cu system. Inferred absolute path lengths from estimates by fitting the Bragg edges alone systematically underestimated (70%) the calculated geometric values. The origin of the underestimation is most likely to be the limited fitting range in the vicinity of the lowest Bragg edges which is strongly dependent on microstructural properties, texture, extinction, etc. The inferred absolute path lengths have been improved using a restricted-region Rietveld-type profile fitting approach. The method has been able to detect absolute path lengths in a very basic two-phase test object with an accuracy of approximately 90% for the majority phase Fe, but slightly worse for the Cu phase, but which has allowed pixel-by-pixel analysis to be performed. Considering that the test object was constructed using conventional engineering materials with impurities and texture, this value is quite promising. It is believed that by using more comprehensive analysis methods, involving more and better models for the cross sections, this value can still be improved. On the other hand, relative path lengths have shown to be in very good agreement with expectations, as was to be expected from previous applications of the transmission technique to monitor phase transformations. The counting time of around 15 min per sample position is fairly good by neutron diffraction standards, and has been sufficient to have basic pixel-by-pixel phase analysis of the 80 live detector pixels, which opens up the possibility of using this method in a tomographic mode, with reasonable data collection times where many such spectroscopic images have to be collected. The use of software filters in the data analysis has been successfully employed to render radiographs of the individual phases, demonstrating the capability of the technique for energy-resolved radiography.

ACKNOWLEDGMENTS

The authors wish to acknowledge the financial support from the EPSRC on Grant Nos. GR/L62801 and GR/L62498, P. Ledgard (OU) for preparing the samples, and M.R. Daymond and J. Quinta da Fonseca for help and support during the experiment. P.J. Withers acknowledges support of Royal Society-Wolfson Merit Award. We would like to thank J.R. Granada for making the software code CRIPO available to us. Also, the FaME38 project at the ESRF-ILL, Grenoble, is gratefully acknowledged for its hospitality.

[1] G. Bacon, *Neutron Diffraction*, 3rd ed. (Clarendon, Oxford, 1975).
[2] E. Fermi, W. J. Sturm, and R. G. Sachs, Phys. Rev. **71**, 589 (1947).
[3] R. G. Johnson and C. D. Bowman, AIP Conf. Proc. **89**, 53 (1982).
[4] C. G. Windsor, *Pulsed Neutron Scattering* (Wiley, London, 1985).
[5] N. Sakamoto, Y. Kiyanagi, S. Sato, H. Sagehashi, M. Furusaka, J. Suzuki, K. Littrell, C. Loong, A. Gorin, I. Manuilov *et al.*, J. Appl. Crystallogr. **36**, 820 (2003).
[6] K. Meggers, H. G. Priesmeyer, W. G. Trela, and M. Dahms, Mater. Sci. Eng., A **188**, 301 (1994).
[7] M. A. M. Bourke, J. G. Maldonado, D. Masters, K. Meggers, and H. G. Priesmeyer, Mater. Sci. Eng., A **221**, 1 (1996).
[8] S. Vogel, E. Ustundag, J. C. Hanan, V. W. Yuan, and M. A. M. Bourke, Mater. Sci. Eng., A **333**, 1 (2002).
[9] J. R. Santisteban, L. Edwards, M. E. Fitzpatrick, A. Steuwer, and P. J. Withers, Appl. Phys. A: Mater. Sci. Process. **A75**, 1 (2002).
[10] H. M. Rietveld, J. Appl. Crystallogr. **2**, 65 (1969).
[11] A. Steuwer, J. R. Santisteban, P. J. Withers, and L. Edwards, Physica B **350**, 159 (2004).
[12] C. G. Windsor and M. Hutchings, *Methods of Experimental Physics* (Academic, New York, 1987), Vol. 23 C.
[13] K. H. Beckurtz and K. Wirtz (1964).
[14] O. Halpern, M. Hamermesh, and M. H. Johnsen, Phys. Rev. **59**, 981 (1941).
[15] W. Marshall and S. W. Lovesey, *Theory of Thermal Neutron Scattering* (Oxford University Press, Oxford, 1971).
[16] J. R. Granada, Z. Naturforsch. Teil A **39a**, 1160 (1984).
[17] P. Hiismäki, J. Appl. Crystallogr. **22**, 79 (1989).
[18] F. Kropff, J. R. Granada, and R. E. Mayer, Nucl. Instrum. Methods Phys. Res. **198**, 515 (1982).
[19] A. Steuwer, J. R. Santisteban, P. J. Withers, L. Edwards, M. E. Fitzpatrick, M. R. Daymond, M. W. Johnson, G. Bruno, and D. Wang, Phys. Status Solidi A **185**, 221 (2001).
[20] J. D. Jorgenson, D. H. Johnson, M. Mueller, S. W. Peterson, T. G. Worlton, and R. B. Von Dreele, in *Proceedings of the Conference on Diffraction Profile Analysis, Cracow 14–15 August 1978*, pp. 20–22 (1978).
[21] R. B. Von Dreele, J. D. Jorgensen, and C. G. Windsor, J. Appl. Crystallogr. **15**, 581 (1982).
[22] G. S. Pawley, J. Appl. Crystallogr. **14**, 357 (1981).
[23] D. Louër, Acta Crystallogr., Sect. A: Found. Crystallogr. **54**, 922 (1998).
[24] R. J. Hill and C. J. Howard, J. Appl. Crystallogr. **20**, 467 (1987).
[25] A. K. Freund, Nucl. Instrum. Methods Phys. Res. **213**, 495 (1983).
[26] G. Squires, Proc. R. Soc. London, Ser. A **212**, 192 (1952).
[27] J. R. Santisteban, L. Edwards, M. E. Fitzpatrick, A. Steuwer, P. J. Withers, M. R. Daymond, M. W. Johnson, N. Rhodes, and E. Schooneveld, Nucl. Instrum. Methods Phys. Res. A **481**, 765 (2002).
[28] K. Binder, Phys. Status Solidi **41**, 767 (1970).
[29] Z. Tabatabaian and N. Spyrou, Nucl. Instrum. Methods Phys. Res. A **424**, 252 (1999).